

## **Zero field Splittings in metHb and metMb with aquo and fluoro ligands: a FD-FT THz-EPR Study**

Joscha Nehrkorn

*Institut für Silizium-Photovoltaik, Helmholtz-Zentrum Berlin für Materialien und Energie, Berlin, Germany and Berlin Joint EPR Laboratory*

Berta M . Martins

*Institut für Biologie, Humboldt-Universität zu Berlin, Berlin, Germany*

Karsten Holldack

*Institut für Methoden und Instrumentierung der Forschung mit Synchrotronstrahlung, Helmholtz-Zentrum Berlin für Materialien und Energie, Berlin, Germany*

Stefan Stoll

*Department of Chemistry, University of Washington, Seattle, USA*

Holger Dobbek

*Institut für Biologie, Humboldt-Universität zu Berlin, Berlin, Germany*

Robert Bittl

*Fachbereich Physik, Freie Universität Berlin, Berlin, Germany and Berlin Joint EPR Laboratory*

Alexander Schnegg

*Institut für Silizium-Photovoltaik, Helmholtz-Zentrum Berlin für Materialien und Energie, Berlin, Germany and Berlin Joint EPR Laboratory*

*Institut für Silizium-Photovoltaik, Helmholtz-Zentrum Berlin für Materialien und Energie, Kekuléstrasse 5, D-12489 Berlin, Germany*

[Alexander.schnegg@helmholtz-berlin.de](mailto:Alexander.schnegg@helmholtz-berlin.de)

(\*) Disclaimer: The publisher's version overrides in case of any discrepancy.

Combined X-band and Frequency-Domain Fourier-Transform THz-EPR (FD-FT THz-EPR) has been employed to determine heme Fe(III)  $S = 5/2$  zero field splitting (ZFS) parameters of frozen solution metHb and metMb, both with fluoro and aquo ligands. Frequency domain EPR measurements have been carried out by an improved synchrotron based FD-FT THz-EPR spectrometer. ZFS has been determined by the field dependence of spin transitions within the  $m_S = \pm 1/2$  manifold, for all four protein systems, and by zero field spin transitions between  $m_S = \pm 1/2$  and  $m_S = \pm 3/2$  levels, for metHb and metMb fluoro-states. FD-FT THz-EPR data were simulated with a novel numerical routine based on *Easyspin*, which allows now for direct comparison of EPR spectra in field and frequency domain. We found purely axial zero field splittings of:  $D = 5.0(1) \text{ cm}^{-1}$  (fluoro-metMb),  $D = 9.2(4) \text{ cm}^{-1}$  (aquo-metMb),  $D = 5.1(1) \text{ cm}^{-1}$  (fluoro-metHB) and  $D = 10.4(2) \text{ cm}^{-1}$  (aquo-metHb).

Keywords: haemoglobin, myoglobin, EPR spectroscopy, zero field splitting

## 1. Introduction

Haemoglobin (Hb) and myoglobin (Mb) attract significant attention because of their central role as oxygen transporters in cellular respiration [1, 2]. In their deoxygenated states, Hb (deoxy-Hb) and Mb (deoxy-Mb) contain heme cofactors with high-spin (HS,  $S = 2$ ) Fe(II). Both reversibly bind oxygen forming diamagnetic oxygenated states (oxy-Hb and oxy-Mb). Oxidation of the ferrous ion yields high spin ( $S = 5/2$ ) Fe(III), usually referred to as metHb and metMb. Fig. 1 depicts the Mb heme structure, together with the orientation of the magnetic anisotropy axis of Fe(III). Mb contains one heme site per protein molecule, whereas Hb contains four. In fluoro derivatives the oxygen at the sixth ligation position is replaced by a fluoride ion. In the following, we refer to systems with fluoro ligands as metHb(F) and metMb(F) and those with aquo ligands as metHb and metMb.

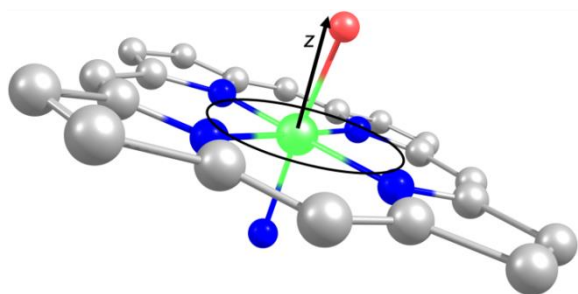


Fig. 1: Heme structure in metMb [3] depicted together with the magnetic hard axis (arrow) and easy plane (circle), C:grey, N:blue, O: red, Fe: green spheres. For metMb the easy plane coincides with the plane of the ligand nitrogens [4]. For metHb, metHb(F), and metMb(F) the z-axis, and the easy plane might be tilted up to  $5^\circ$  from the shown orientation [4].

Despite the fact that these proteins are among the best studied biomolecules, the electronic and magnetic structures of their function determining heme sites are still not fully understood. The ideal technique for studying paramagnetic transition metal ions (TMI), like Fe(II) and Fe(III), is electron paramagnetic resonance (EPR) [5]. Indeed, several ground breaking EPR studies on Fe(II) and Fe(III) states in Mb and Hb, yielded important insight into their magnetic structure function relationship. Examples that stand out are the determination of the heme group orientations in metMb [6] and metHb [7] even before crystal structures were available. Later studies employed the HS Fe(III) g-tensor anisotropy as finger print [4, 8]. Additional important structural information may be extracted from studies in the iron zero field splitting tensors (ZFS).

However, in the case of HS TMI with large ZFS such studies are challenging. Even though Fe(II) is paramagnetic, it cannot be detected by conventional EPR. The reason for this is the large ZFS between the magnetic sublevels of HS states [9-11]. Fe(III) is accessible by conventional EPR [6, 7], but again advanced variable frequency EPR is required to precisely determine its ZFS. In both systems ZFS is of particular interest since it reflects the heme ligand structure including the binding site for dioxygen. The

sensitivity of the ZFS on the coordination sphere may be demonstrated by replacing the water molecule in the axial ligand position of metMb/Hb with a fluoride ion (see Fig. 1), which yields again HS Fe(III), but with strongly reduced ZFS [12].

Magnetic properties of HS ( $S > 1/2$ ) TMIs, exposed to an external magnetic field, without first-order orbital momentum, may be expressed by the following general spin Hamiltonian (SH) [13, 14]:

$$\hat{\mathbf{H}} = \mu_{\text{B}} \mathbf{B}_0 \cdot \mathbf{g} \cdot \hat{\mathbf{S}} + \hat{\mathbf{S}} \cdot \mathbf{D} \cdot \hat{\mathbf{S}} \quad 1$$

Here, the first term denotes the Zeeman interaction, which couples  $\hat{\mathbf{S}}$  to the external magnetic field  $\mathbf{B}_0$  via the anisotropic g-tensor,  $\mathbf{g}$ . The second term describes the local crystal field or ZFS term parameterized by the ZFS tensor,  $\mathbf{D}$ . ZFS lifts the degeneracy of the  $2S + 1$  magnetic sublevels, even in the absence of an external magnetic field. It may result from two contributions [15, 16]: (a) dipole–dipole interactions of open-shell electron spins (to first order in perturbation theory) and (b) spin–orbit coupling. ZFS may be expanded in a series of magnetic multipoles [17],

$$\hat{\mathbf{H}}_{\text{ZFS}} = \hat{\mathbf{S}} \cdot \mathbf{D} \cdot \hat{\mathbf{S}} = D(\hat{S}_z^2 - S(S+1)/3) + E(\hat{S}_x^2 - \hat{S}_y^2) \quad 2$$

where  $D$  and  $E$  are the axial first order and the transverse second order terms [18], respectively.

$$D = D_{zz} - \frac{1}{2}(D_{xx} + D_{yy}) \quad 3$$

$$E = \frac{1}{2}(D_{xx} - D_{yy}) \quad 4$$

Thereby, the major anisotropy axis is chosen as quantization axis (see Fig. 1). In spin systems with  $D > 0$ , like metMb and metHb, this is the hard axis, because energy is required to reach parallel alignment between spin and quantization axis. Spin alignment in the perpendicular plane is energetically favourable, hence it is called easy plane. SHs provide a handy way to model magnetic TMI properties and simulate their EPR spectra.

Diagonalization of Eq. 1 yields spin energy levels. EPR resonances occur when the sample is exposed to microwave (mw) quanta matching the energy difference between two spin eigenstates. EPR intensities are determined by population differences between these states as well as the transition probability between spin eigenstates induced by the oscillating magnetic field. The probabilities determine the EPR selection rules ( $\Delta S = 0$ ,  $\Delta m_S = \pm 1$ , with  $m_S$  being the expectation value of  $\hat{S}_z$ ). Due to instrumental reasons, the large majority of EPR experiments are carried out at fixed mw frequency by varying the external magnetic field. Hence, most EPR simulation programs calculate field domain spectra. However, frequency-domain calculations are superior to their field domain analogues, with respect to computational costs. Frequency domain spectra may be obtained by a single diagonalization of Eq. 1, whereas field domain simulations require diagonalizations for many field points.

To reduce the number of field points necessary to achieve high fidelity and to locate all resonances within a range, sophisticated interpolations schemes have been implemented [19]. This becomes important for systems with very large total spins or many coupled spins. Numerical diagonalization of such SH matrices can become very costly, leading to a clear advantage of the frequency domain approach in this case.

Fig. 2 depicts calculated [19] spin energy levels for an  $S = 5/2$  system with large positive axial ZFS ( $D = 10 \text{ cm}^{-1}$ ,  $E = 0$ , isotropic  $g = 2.0$ ), plotted against the external magnetic field ( $B_0$ ) [19]. This is the case for Fe(III) in metMb/Hb [12]. In zero magnetic field the energy levels are split by ZFS into Kramers doublets. Under these conditions axial ZFS may be directly extracted by measuring the ground state  $\pm 1/2$  to  $\pm 3/2$  EPR transition energies  $\Delta E = 2D$  (Fig. 2 blue line in the lower right box). This transition has been employed to determine  $D$  in metMb(F) and metHb(F), but similar attempts on the aquo forms metMb and metHb failed [12]. In the presence of an external magnetic field spin

energy levels are further split by the Zeeman interaction and EPR resonances at lower transition energy become allowed.

Splitting of the energy levels depends on the size and the orientation of  $\mathbf{B}_0$  relative to the principal axes of the ZFS tensor (see Fig. 1). For  $\mathbf{B}_0$  parallel to the molecular  $z$  axis, the Zeeman interaction increases the splittings linearly with  $B_0$ , because the eigenstates of Eq. 1 are eigenstates of  $\hat{S}_z$  (black lines in Fig. 2). For  $\mathbf{B}_0$  oriented perpendicular to the molecular  $z$  axis, states differing by  $\Delta m_S = \pm 1$  are mixed. The result is nonlinear  $B_0$  dependence of the energy levels (green lines in Fig. 2).

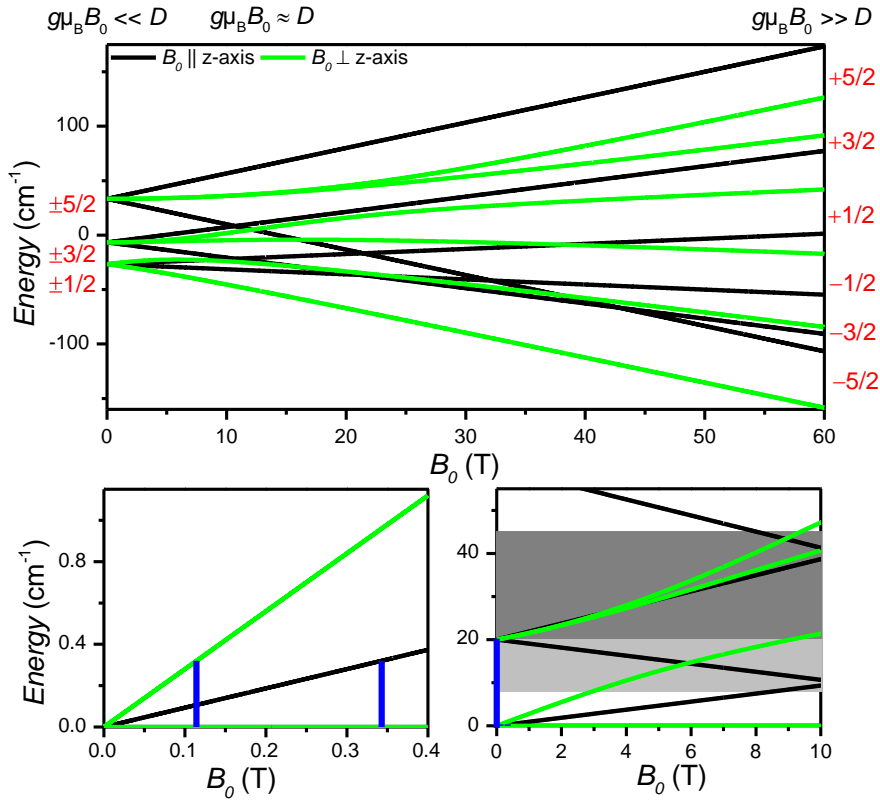


Fig. 2: Calculated spin energy levels for  $S = 5/2$  ( $D = 10 \text{ cm}^{-1}$ ,  $E = 0$ ), as a function of  $B_0$ . Energy levels for external magnetic fields aligned parallel to the hard axis (see Fig. 1) are shown in black. Green lines indicate levels for perpendicular (in the easy plane) field orientation. In the top panel  $m_S$  quantum numbers (red) are indicated for low field ( $g\mu_B B_0 \ll D$ , left) and high field limits ( $g\mu_B B_0 \gg D$ , right). The lower panels depict enlarged views of the ground state energy levels in the low field (left panel) and intermediate field

limit ( $g\mu_B B_0 \approx D$ , right panel). In both lower panels, energy levels are shown as energy difference to their respective ground state. In the lower left panel allowed X-band (9 GHz /  $0.3 \text{ cm}^{-1}$ ) transitions within the ground state  $m_S$  manifold are depicted by blue lines. The blue line in the lower right panel indicates  $m_S = \pm 1/2$  to  $\pm 3/2$  EPR transitions at zero magnetic field. Obviously, X-band quanta are insufficient to span this large energy gap. The energy window in which excitations from the ground state can be observed by FD-FT THz EPR is indicated by grey bars. Depending on the overall absorption of the studied sample the highest detectable energies vary between  $20 \text{ cm}^{-1}$  (strongly absorbing samples, light grey) and  $45 \text{ cm}^{-1}$  (slightly absorbing samples, dark grey).

In the low field limit,  $g\mu_B B_0 \ll D$ , resonances within the ground state doublet can be modelled by an effective  $S = 1/2$  with  $g_{\parallel}^{\text{eff}} = g_{\parallel} \approx 2$  and  $g_{\perp}^{\text{eff}}$  given by [8]

$$g_{\perp}^{\text{eff}} = 3g_{\perp} \left[ 1 - 2 \left( \frac{g_{\perp} \mu_B B_0}{2D} \right)^2 \right] \quad 5$$

Hence, the field dependence of  $g_{\perp}^{\text{eff}}$  provides an easy way to determine  $D$ , even in cases when the applied microwave energy is not sufficient to excite zero field ground state transitions. However, Eq. 5 reproduces the field dependence of the spin energy levels only in a relatively narrow range in the low field regime. More reliable information may be obtained by simulations based on a full matrix diagonalization of Eq. 1. The slope of  $g_{\perp}^{\text{eff}}$  as a function of  $B_0$  was employed in several studies, to extract  $D$  in metMb [4, 8], metMb(F) [4], and metHb [20]. A summary of ZFS and g-values obtained by different methods is given in Tab. 1. The method with the highest accuracy for the determination of large ZFS is EPR. However, due to limited excitation energies/powers or external magnetic fields, recent EPR studies reported largely varying ZFS values. In addition, none of the recent studies succeeded in determining ZFS in metMb and metHb and its fluoro states in one single study. Very recently we demonstrated that Frequency-Domain Fourier-Transform THz-EPR (FD-FT THz-EPR) based on coherent synchrotron radiation

(CSR) at THz frequencies [21] provides a unique tool that goes beyond the restrictions of other EPR techniques. This novel approach allows for EPR excitations over a broad energy ( $7\text{ cm}^{-1} - 45\text{ cm}^{-1}$ ) and magnetic field ( $-11\text{ T}$  to  $11\text{ T}$ ) range in a single spectrometer and with a single source [21]. The power of FD-FT detected EPR for studying high spin iron compounds, including metHb and metMb, was demonstrated in an early ground breaking study by Brackett and co-workers [12]. However, at that time CSR was not yet available and magnetic fields were limited to  $5\text{ T}$ .

In the present study, we employ FD-FT THz-EPR to determine  $D$  of metMb and metHb with aquo as well as with fluoro ligands. In the following we will describe the sample preparation used and FD-FT THz-EPR measurement protocols, present FD-FT THz-EPR and X-band EPR data on metHb and MetMb, extract their ZFS by a novel spectral simulation routine and finally discuss the results together with an outlook on the perspectives and challenges of future ultra-wide band FD-FT THz-EPR studies on metalloproteins.

## **2. Experimental Methods**

### ***2.1. Sample preparation***

metHb and matMb were purchased from Sigma-Aldrich as lyophilized powders. Absorption spectra in the UV and visible region were recorded for the FD-FT THz-EPR samples to check their concentrations using the molar extinction coefficients tabulated in [22]. UV-visible spectra were recorded using an Agilent 8453 diode array spectrophotometer.



#### *metHb and metMb X-Band*

Hb was dissolved in 10 mM (NH<sub>4</sub>)-phosphate pH 7.0 buffer as a 2 % (weight/volume) solution. The solution was concentrated with a Millipore concentrator (30 kDa cut-off) at 2200 rpm to approximately 4 %. 5  $\mu$ L of a 300 mM K<sub>3</sub>[Fe(CN)<sub>6</sub>] solution were added to 500  $\mu$ L of the concentrated Hb solution. The solution was then filtered using Nylon 0.45  $\mu$ m Millipore Millex HN filters and buffer exchanged to 10 mM (NH<sub>4</sub>)-phosphate pH 7.0 using Sephadex G-25. The filtered solution was concentrated again to around 4 %, filled in EPR quartz tubes and immediately frozen in liquid nitrogen. The same procedure was used for metMb X-Band samples where Mb from horse skeletal muscle was used.

#### *metHb FD-FT THz*

1.5 g of Hb was dissolved in 75 mL 150 mM Na/K-phosphate pH 7.0 buffer to have a 2% (weight/volume percent) solution. The solution was stirred for around 3 hours. After 1.5 mL of 300 mM K<sub>3</sub>Fe(CN)<sub>6</sub> was added to this solution, it was stirred for another 1 hour and filtered using Nylon 0.45  $\mu$ m Millipore Millex HN filters. The solution was equilibrated 3 times through dialysis against 15 L of 150 mM Na/K-phosphate pH 7.0 buffer. The metHb solution was finally concentrated using a Millipore concentrator (30 kDa cutoff) at 2200 rpm and from the remaining 5 mL approximately 2 to 3 mL were filled in a THz sample cup (hollow Teflon cylinders) and immediately frozen in liquid nitrogen. The sample was defrosted and slowly frozen again in order to avoid occlusion of air bubbles in the sample can. For this sample a concentration of 21(1) mM heme was determined from UV-vis measurements.

#### *metHb(F) FD-FT THz*

1.5 g of Hb was dissolved in 75 mL of 10 mM (NH<sub>4</sub>)-phosphate pH 7.0 containing 1 M NaF. 1.5 mL of 300 mM K<sub>3</sub>Fe(CN)<sub>6</sub> was added and after a few minutes incubation the

solution was filled in a Millipore concentrator (30 kDa cut-off) and concentrated at 2200 rpm to a final volume of circa 7 mL. After 3-4 hours the concentrator was filled up with NaF containing buffer and concentrated again to approximately 5 mL. The last step was repeated once. Prior to the final concentration step the solution was filtered using Nylon 0.45  $\mu$ m Millipore Millex HN filters. About 2 to 3 mL of the final solution was filled in a THz sample cup and immediately frozen in liquid nitrogen. A concentration of 11(2) mM heme was determined from UV-vis measurements.

#### *metMb and metMb(F) FD-FT THz*

0.5 g of Mb from horse skeletal muscle was added to 1 mL buffer solution. For the Mb sample the buffer was 150 mM sodium hydrogen phosphate pH 7.0, for which  $\text{NaH}_2\text{PO}_4$  and  $\text{Na}_2\text{HPO}_4$  solutions were mixed to obtain a pH value of 7.0. The metMb(F) was prepared with the same buffer containing 1 M NaF. Concentrations of 20(3), and 22(2) mM heme were determined from UV-vis measurements for the metMb and the metMb(F) sample, respectively.

### **2.2. X-band EPR**

EPR was performed on a Bruker ESP 300 X-band EPR spectrometer equipped with He cooled sample cryostat and a TE011 super high Q microwave resonator.

### 2.3.FD-FT THz-EPR

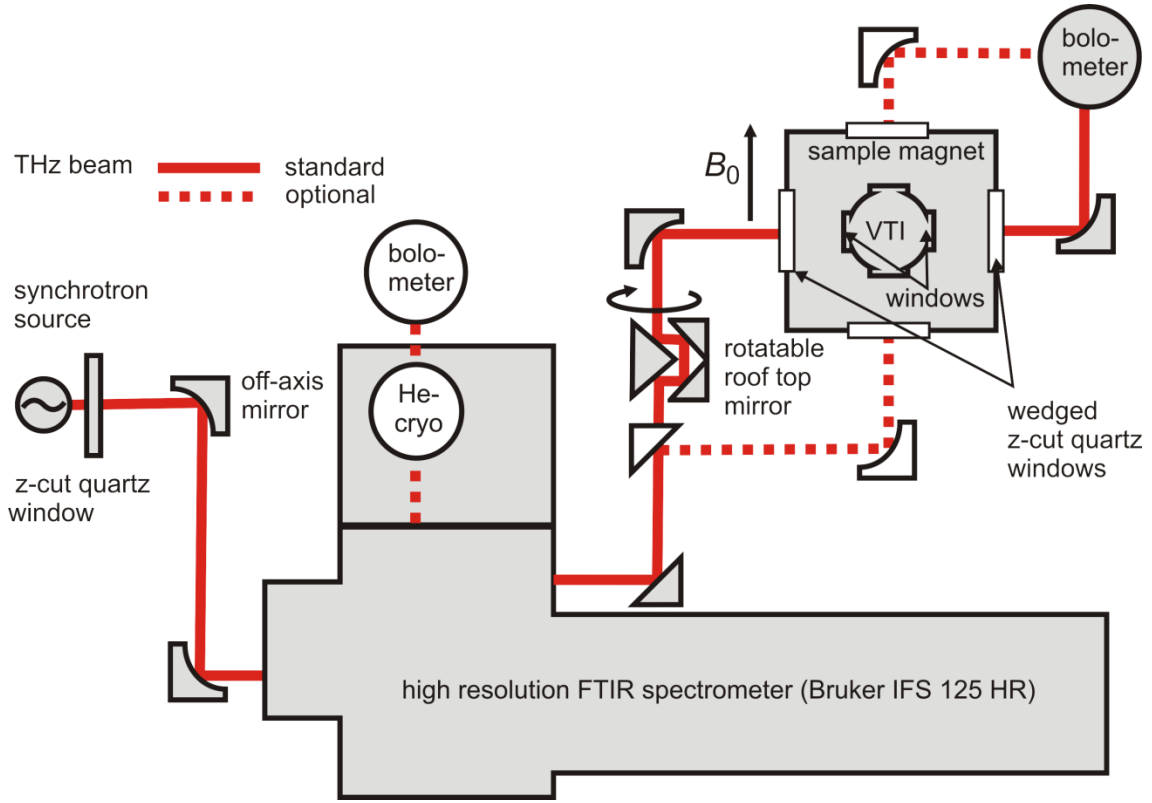


Fig. 3: FD-FT THz-EPR detection scheme.

Fig. 3 depicts a scheme of the FD-FT THz-EPR spectrometer installed at the electron storage ring BESSY II. In the spectrometer intense broad-band CSR [23], in the THz range, is extracted from the radiation outlet on top of the storage ring, through a z-cut quartz window. The THz beam (depicted in red) is further transmitted by an evacuated low-loss quasi-optical transmission line and focused on the external radiation port of a high resolution FTIR-spectrometer (Bruker IFS 125, min. bandwidth:  $0.0063 \text{ cm}^{-1}$ ), by off-axis parabolic mirrors. After passing through the spectrometer, the radiation again propagates through a vacuum sealed quasi-optical beam line, which focuses the THz radiation onto the windows of a sweepable superconducting magnet (Oxford Spectromag). The split-coil magnet is equipped with four outer wedged z-cut quartz windows. In the standard configuration (Voigt geometry, solid red line)  $B_0$  is oriented

perpendicular to the propagation direction of the radiation. In the magnet housing a variable temperature insert (VTI) equipped with additional four z-cut quartz windows is immersed. This configuration allows for measurements from  $T = 1.5$  K to 300 K, at external magnetic fields variable between -11 and +11 T. The evacuated beam line incorporates a rotatable roof-top mirror, which acts as broad band polarization shifter [24]. This device allows for orienting the magnetic component of the linearly polarized THz radiation ( $B_1$ ) parallel or perpendicular to the static magnetic field ( $B_0$ ). Alternatively, the radiation may be guided through the second pair of magnet windows (Faraday geometry) or to an additional optical cryostat (Oxford-Optistat,  $T = 1.5$  K- 300 K) inside the FTIR spectrometer (dotted red lines).

The configuration with the optical cryostat provides higher overall THz intensities, due to a smaller number of windows, separating the different compartments, and higher sample throughput. In all three configurations, highly sensitive detection is achieved by liquid helium-cooled InSb and Si bolometers, as well as by pyroelectric crystal based detectors. Si bolometers provide the highest overall detection sensitivity ( $10^{-13}$  to  $10^{-14}$  W/Hz<sup>1/2</sup>) as compared to the other detectors. InSb bolometers on the other hand exhibit the fastest response times (1 MHz for InSb as compared to 400 Hz for Si). This allows for sensitive lock-in detection up to MHz frequencies. In our set-up amplitude modulated lock-in detection can be realised by employing the CSR time structure. As the THz radiation is emitted and modulated by the electron bunches in the storage ring, the detection can be locked on the repetition rate of the electron macro bunches (1.25 MHz) [21]. In the case of concentrated protein samples with very high broad band THz absorption we found that the high sensitivity of Si bolometers provide FD-FT THz-EPR spectra with optimum signal-to-noise ratio (S/N).

FD-FT THz-EPR has been successfully applied to single molecule magnets [21, 25-27] and mononuclear integer HS TMIs [28] to extract their ZFS. The achievable S/N as well as the accessible frequency range strongly depend on nonmagnetic extinction of the THz beam in the sample. Reduction of the THz intensity can be due to reflections on the sample surface, absorption by collective motion in the sample or scattering and diffraction for powder samples. Depending on the spectral width and the optical sample properties a maximum sensitivity of  $5 \times 10^{19} - 1 \times 10^{18}$  spins in the sample was achieved so far. Since CSR intensity is frequency dependent, the noise floor of the set-up varies as a function of frequency (viz. excitation energy). This is demonstrated for a frozen solution sample of metMb(F) in Fig. 4. Raw spectra were obtained by FT detection of CSR THz emission spectra through the empty magnet VTI (Fig. 4, gray dashed line) and with a 10 mm thick frozen metMb(F) solution (heme conc. 22 mM). Raw spectra of protein were recorded at different temperatures and external magnetic fields. Raw spectra taken without sample mainly reflect the spectral shape of radiation emitted by the synchrotron and the standing wave pattern of the quasi optical beam path. The latter leads to pronounced modulations on the raw spectra and a cut-off at the low frequency edge of the spectrum ( $\sim 7 \text{ cm}^{-1}$ ). Raw spectra of protein are dominated by intense broad band optical absorption of the protein sample in this frequency range, which increases with increasing frequency [10, 12]. In the raw spectra of metMb(F) shown in Fig. 4 the measured intensity is almost zero for energies greater than  $20 \text{ cm}^{-1}$ .

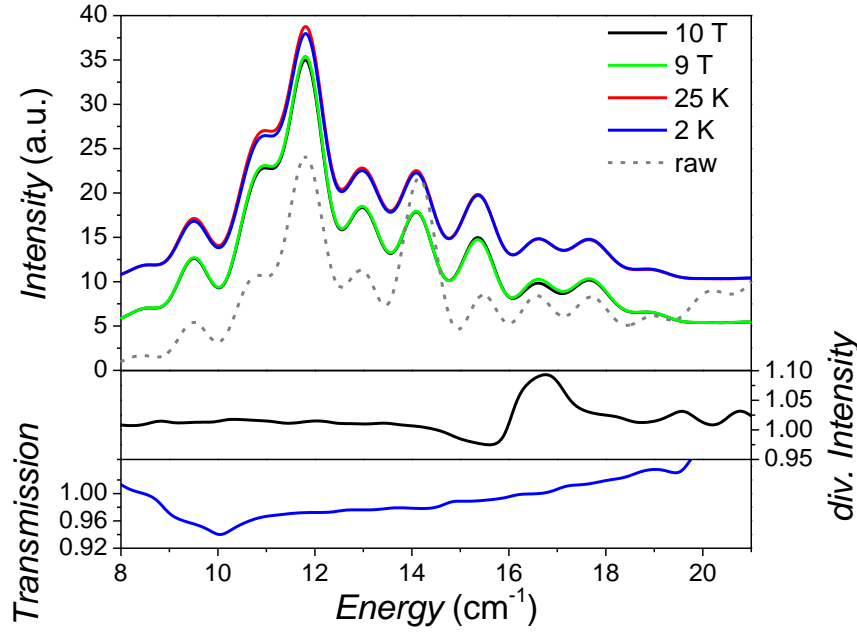


Fig. 4 Upper box: raw THz spectra taken without sample (dashed gray line) at room temperature and with a 10 mm thick sample of frozen metMb(F) solution (heme conc. 22 mM). metMb(F) spectra were recorded without external magnetic field at  $T = 2$  K (blue) and 25 K (red). In addition, spectra taken at  $T = 2$  K with applied external magnetic fields of 9 T and 10 T (green and black line, respectively) are displayed. metMb(F) raw spectra are shown with an offset. The raw spectrum without sample was downscaled by a factor of 100. Lower boxes: FD-FT THz-EPR spectra obtained by dividing low temperature spectra taken at 9 T and 10 T (black line, middle box) and by dividing zero field spectra taken at 2 K and 25 K (blue line, bottom box). Experimental conditions: THz source: synchrotron in low  $\alpha$  mode, synchrotron ring current ( $I_{\text{ring}}$ ) 100 mA, detector: LHe cooled Si-bolometer, spectral resolution:  $0.5 \text{ cm}^{-1}$ , data acquisition time per spectrum: 30 minutes.

From raw spectra FD-FT THz-EPR spectra may be obtained in two ways: First, by dividing low temperature (e.g. 2 K) spectra by spectra taken at elevated temperatures (e.g. 30 K). Thereby, changes in the population of the spin energy levels may be recorded as EPR induced transmission changes. This method can be used even without external magnetic field and was used successfully in several studies [10, 12, 21, 25-28]. However, many non-magnetic absorption processes also depend on temperature, which are

sometimes difficult to distinguish from spin transitions. Alternatively, reference spectra may be obtained by taking raw spectra at different magnetic fields. These two strategies are shown in the lower boxes of Fig. 4. The blue line was obtained by dividing zero magnetic field raw spectra taken at  $T = 2$  K and 25 K. The black line shown in the middle box of Fig. 4 was obtained by dividing raw spectra taken at 9 T and 10 T at fixed temperature ( $T = 2$  K). Minima in the divided intensity indicate ground state spin transitions at 9 T, while maxima indicate ground state spin transitions at 10 T.

In the following we will refer to this method as field division method. Its main advantage is that temperature induced non-magnetic transmission changes can be avoided by taking reference spectra at the same temperature, but altered magnetic field. This method was validated by measuring a TEMPO standard sample (30 mg of TEMPO mixed with an equal mass of Teflon and pressed to a pellet). For comparison, experimental and simulated field division FD-FT THz-EPR spectra of TEMPO and metMb(F) are depicted in the left and right panel of Fig. 5, respectively.

For TEMPO with  $S = 1/2$  and known SH parameters [29], we received sharp minima and maxima by dividing spectra taken at 9 T and 9.1 T. The observed Gaussian line width is dominated by the chosen experimental resolution of  $0.05 \text{ cm}^{-1}$  (1.5 GHz) and not by the width of the TEMPO powder spectrum ( $\sim 1.1 \text{ GHz} / 0.037 \text{ cm}^{-1}$  at 9 T). Nevertheless, sharp lines observed for TEMPO clearly demonstrate that the width of  $0.8 \text{ cm}^{-1}$ , observed for the protein samples, are not due to instrumental restrictions but intrinsic sample properties. The much weaker transmission in the metMb(F) sample, as compared to TEMPO, demonstrate the challenge of FD-FT THz EPR on proteins.

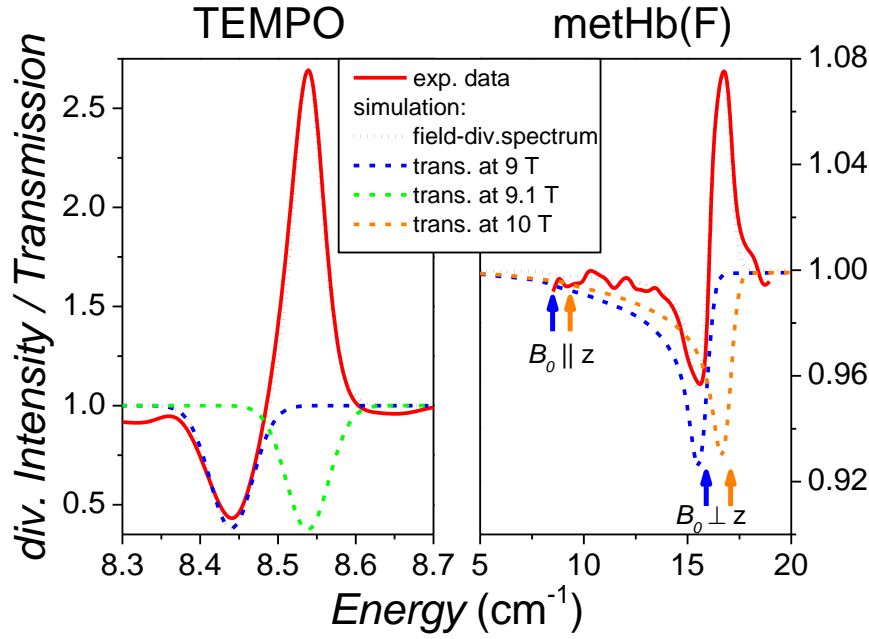


Fig. 5: Left: Experimental (red solid line) field division FD-FT THz-EPR spectrum obtained from FD-FT raw spectra of TEMPO measured at magnetic fields of  $B_0 = 9$  T and 9.1 T. Experimental conditions: THz source: synchrotron in low  $\alpha$  mode,  $I_{\text{ring}} = 100$  mA, detector: LHe cooled Si-bolometer, spectral resolution:  $0.05 \text{ cm}^{-1}$  (1.5 GHz), data acquisition time per spectrum: 10 minutes,  $T = 5$  K. Transmission spectra simulated for  $B_0 = 9$  T (blue dashed line) and 9.1 T (green dashed line) (simulation parameters:  $S = 1/2$ , isotropic  $g = 2.0034$ , Gaussian line width:  $0.064 \text{ cm}^{-1}$ ) and the resulting simulated field division spectrum (black dotted line). Right: Experimental field division FD-FT THz-EPR spectrum (red solid line) of metMb(F) obtained from raw spectra measured at 9 T and 10 T (see Figure 3), together with simulated transmission (blue (9 T) and orange (10 T) dashed lines) and field-division (black dotted line) spectra. Calculated  $m_S = \pm 1/2$  ground state splittings for parallel and perpendicular  $\mathbf{B}_0$  alignment at  $B_0 = 9$  T and 10 T are indicated by blue and orange arrows, respectively.

#### 2.4. FD-FT THz-EPR and X-band simulations

In order to determine Fe(III) D-values of metMb and metHb FD-FT THz-EPR spectra ranging from  $8 \text{ cm}^{-1}$  to  $21 \text{ cm}^{-1}$  and 0 T to 10 T, were acquired and analysed using a novel frequency-domain simulation extension to the *Matlab* toolbox, *EasySpin* [19]. Based on the capabilities of *EasySpin*, EPR transitions were calculated for the SH given in Eq. 1.



Variations in the local iron environment can lead to variations in the magnetic interaction parameters, in particular **g** and **D** values. This so called g and D strains were considered by folding each transition with a Gaussian, where the line width is given by the magnitude of the derivative of the SH with respect to  $g_{\perp}$  (in the case of  $g_{\perp}$  strain) at the resonance multiplied by the  $g_{\perp}$  strain parameter  $\sigma_{g_{\perp}}$ . Averaging over all sample orientations gives the powder spectrum. Residual Gaussian line width contributions are considered by folding the resulting spectra with Gaussian line width functions.

X-band spectra were also calculated with *EasySpin* routines.

### 3. Results

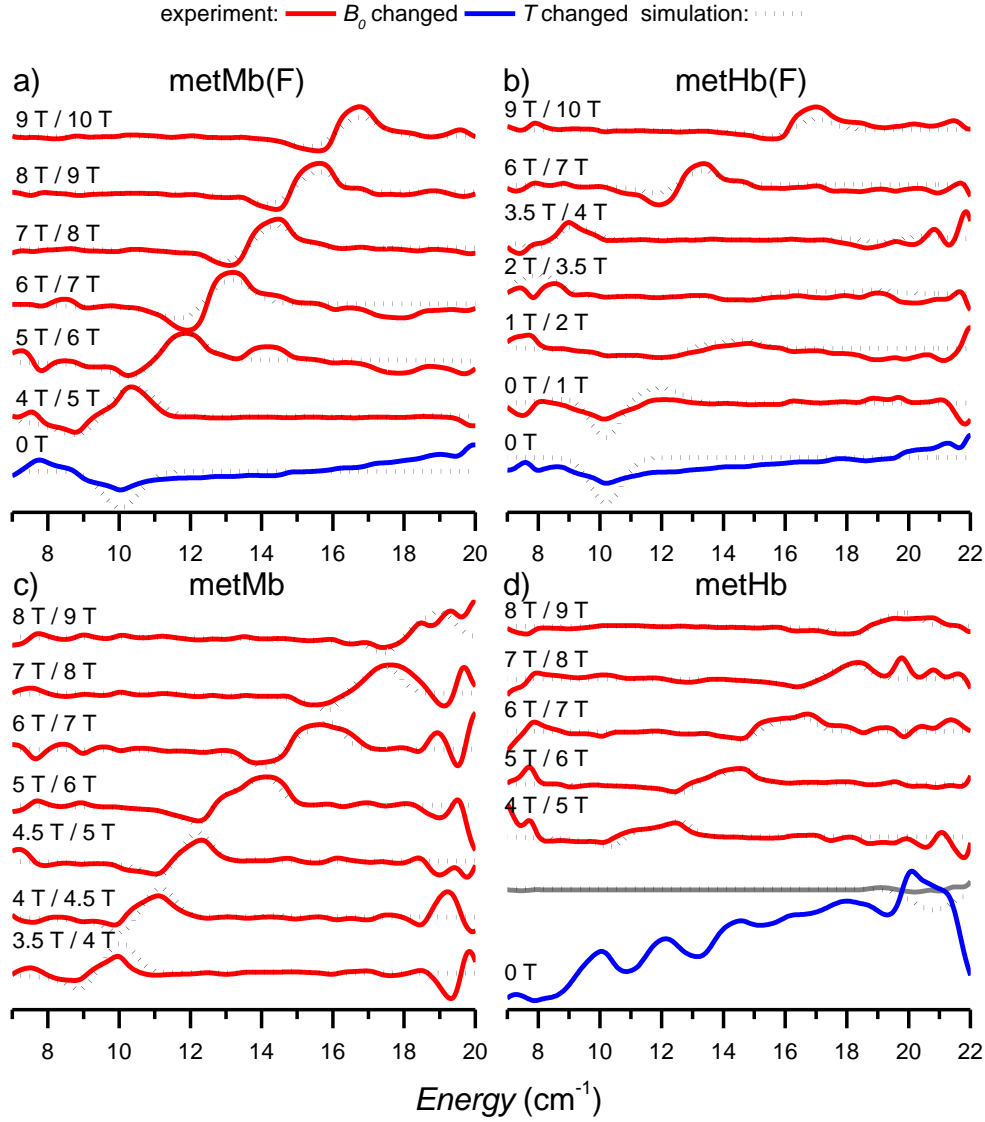


Fig. 6: Temperature (lower blue lines in a), b) and d)) and field division (red lines) metMb(F) (a), metHb(F) (b), metMb (c) and metHb (d) FD-FT THz-EPR spectra. Temperature dependent transmission spectra were obtained by dividing spectra taken at temperatures of 2 K and 25 K (metMb(F)), 2 and 20 K (metHb(F)), and 5 and 40 K (metHb), without external magnetic field. For metHb also an experimental baseline (grey solid line) is shown. Field division spectra were obtained by dividing spectra taken at indicated magnetic fields at  $T = 2$  K. Black dotted lines show simulations with parameters given in Tab. 1. FD-FT THz-EPR spectra are shown with an offset for clarity. Experimental conditions: THz source: synchrotron in low  $\alpha$  mode,  $I_{\text{ring}} = 100$  mA,

detector: LHe cooled Si-bolometer, spectral resolution:  $0.5\text{ cm}^{-1}$ , data acquisition time per spectrum: 30 minutes.

Fig. 6 shows zero-field FD-FT THz-EPR spectra (blue lines) together with field division FD-FT THz-EPR spectra, taken at different external magnetic field strengths (red lines). FD-FT THz-EPR data obtained for metHb and metMb and their respective fluoro derivatives exhibit several pronounced differences. For the fluoro complexes depicted in Fig. 6a) and 6b) a pronounced transmission decrease around  $10\text{ cm}^{-1}$  could be observed upon lowering the temperature at zero magnetic field. For metHb(F) this line shifts to higher energies upon applying an external magnetic field (see 0 T / 1 T and 1 T / 2 T spectra in Fig. 6b)). A similar behavior was observed for metMb(F) (data not shown). Based on these findings, the resonances were assigned to ground state EPR transitions between  $m_S = \pm 1/2$  and  $m_S = \pm 3/2$  manifolds. Aquo states of metMb (data not shown) and metHb (blue line in Fig. 6d)) didn't show this feature. It is worthwhile noting that the zero-field transitions for metMb(F) and metHb(F) are unexpectedly broad and weak, compared to transitions at higher magnetic fields. As a result, it may be difficult to observe them at resonance energies at or above  $20\text{ cm}^{-1}$ , where the transmitted THz intensity decays. For the fluoro as well as for the aquo complexes, above 3 T an additional resonance peak appears which shifts to higher resonance energies upon increasing the external magnetic field. This second peak was assigned to resonances within the ground state  $m_S = \pm 1/2$  doublet. Again fluoro and aquo complexes exhibit different FD-FT THz-EPR spectra, most evident in the high field spectra. For the fluoro complexes, resonances can be recorded up to the maximum field of 10 T, where the resonance energy reaches  $16.5\text{ cm}^{-1}$  (upper red lines in Fig. 6a) ) and 6b)). On the contrary, for the aquo complexes already at 9 T resonances appear at the edge of the observation window at  $20\text{ cm}^{-1}$  (see upper red line in Fig. 6c) and d)). At 10 T no reliable data could be extracted for metMb and metHb (data not shown).

For the field dependent transition within the  $m_S = \pm 1/2$  levels different spectrometer resolutions have been tested for field values between 5 T and 10 T (data not shown). However, no further increase of the spectral resolution could be achieved below  $0.5 \text{ cm}^{-1}$  by improving the FTIR spectrometer resolution. Accordingly, we have chosen a spectral resolution of  $0.5 \text{ cm}^{-1}$ . This is nearly two orders of magnitude larger than the maximum resolution of the FTIR spectrometer (see e.g. Fig. 5). Surprisingly, no line width variation was found, when increasing the external magnetic field.

For the determination of ZFS parameters we performed spectral simulations based on Eq. 1, assuming HS  $S = 5/2$  states in all four cases. Employed simulation strategies are outlined in the following. For metMb(F) and metHb(F) ground state  $m_S = \pm 1/2$  to  $m_S = \pm 3/2$  transitions were observed at  $10.0(2) \text{ cm}^{-1}$  and  $10.2(2) \text{ cm}^{-1}$ , respectively. The corresponding transition energy is  $\Delta E = 2D$  and hence estimates of  $D$  could be obtained. These values were further corroborated by simultaneous simulations of zero field and high field FD-FT THz-EPR spectra. Simulations yielded  $D = 5.0(1) \text{ cm}^{-1}$  and  $g_{\perp} = 2.025(5)$  for metMb(F) and  $D = 5.1(1) \text{ cm}^{-1}$  and  $g_{\perp} = 2.05(1)$  for metHb(F). Variation of  $g_{\parallel}$  had no influence on the simulations, hence it was fixed to 2.0 for both metMb(F) and metHb(F). Using these parameters we calculated FD-FT THz-EPR spectra depicted in Fig. 6a) and b). Gaussian line widths of  $0.8 \text{ cm}^{-1}$  were used to simulate FD-FT THz-EPR results, including zero-field spectra for metMb/Hb both with fluoro and aquo ligand. This value matches the line width of field division spectra quite well, but clearly underestimates the line width of zero field resonances of metMb(F) and metHb(F). In the case of metMb and metHb no clear evidence for a zero field EPR transition could be obtained. Due to this fact,  $D$  had to be determined solely from the slope of the high field EPR resonances depicted in Fig. 6c) and 6d) for metMb and metHb, respectively. In order to increase the quality of the simulations, we employed X-band EPR (see Fig. 7) to

independently determine metMb and metHb  $g$ -values. At low frequencies, and for  $D$ -values as large as expected for metMb and metHb, the observed features are almost independent of  $D$ . X-Band EPR yielded  $g_{\perp} = 1.995(5)$ ,  $g_{\parallel} = 2.019(2)$  for metMb and  $g_{\perp} = 1.989$  and  $g_{\parallel} = 2.0176$  for metHb. Experimental metMb X-band spectra were best reproduced assuming  $g$ -strain (FWHM) of  $\sigma_{g\perp} = 0.05$ ,  $\sigma_{g\parallel} = 0$ , and a residual Gaussian line width (FWHM) of 1.75 mT for metMb. For metHb the data could be best reproduced assuming strains of  $\sigma_{g\perp} = 0.075$  and  $\sigma_{g\parallel} = 0$  and a Gaussian line width of 1.5 mT.

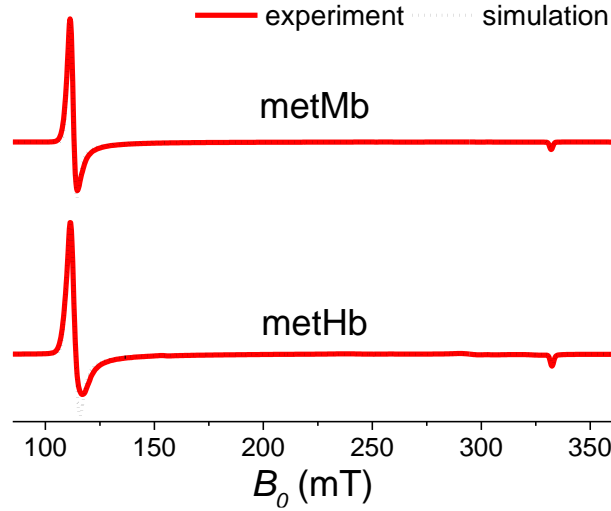


Fig. 7: Experimental (red lines) and simulated (dotted black lines) metMb (top) and metHb (bottom) X-Band EPR spectra taken at  $T = 5$  K. Experimental conditions:  $\nu_{\text{mw}} = 9.383$  GHz (metMb) and 9.388 GHz (metHb),  $P_{\text{mw}} = 0.2$  mW, mod. amp. 0.3 mT (metMb) and 0.5 mT (metHb).

For metMb and metHb only the  $D$ -value was varied in the simulations of FD-FT THz-EPR data. From these simulations we received  $D = 9.2(4)$   $\text{cm}^{-1}$  for metMb and  $D = 10.4(2)$   $\text{cm}^{-1}$  for metHb. The inclusion of  $g$ -strain, determined from X-band EPR, had virtually no influence on the simulated FD-FT THz-EPR spectra and hence it was not considered further in the frequency-domain simulations. The applied simulation routines do not

allow for a direct determination of FD-FT THz-EPR transmission changes. However, based on the applied approach relative changes induced by different fields or temperatures can be modeled. In order to exploit this capability, all simulated spectra of a respective sample were rescaled with the same factor to reproduce the experimental data. Obviously rescaling of each spectrum would lead to better agreement with the experimental data; however the relative intensity changes between different spectra can give additional information about the observed transitions. Two conclusions may be drawn from comparing the spectra. First, the observed  $m_S = \pm 1/2$  transmission shows only little field dependence, which is confirmed by simulations (see red solid and black dotted lines in Fig. 6, respectively). Secondly, the transmission of metMb(F) and metHb(F) at zero magnetic fields is predicted to be much stronger than in the experiment (see lower black dotted and blue lines in Fig. 6a) and 6b), respectively). However, due to the extreme width of the experimental spectrum a quantitative comparison is difficult.

Simulated spectra depicted in Fig. 6 were obtained with purely axial ZFS in all four cases. To validate this assumption, we repeated the simulations with non-axial ZFS. We found that inclusion of  $E$  ( $> 0.01 D$ ) leads to a field dependent line width increase, or even a splitting of the high-field feature, despite the large line width of  $0.8 \text{ cm}^{-1}$ . As this was not observed experimentally, non-axial ZFS was dropped from further considerations. Tab. 1 summarizes SH parameters obtained from simulations depicted in Fig. 6.

Simulation and experiment agree well, with respect to the spectral positions of the EPR resonances. Slight deviations in the high energy range of the spectra ( $> 16 \text{ cm}^{-1}$ ) are due to the increased noise at these spectral positions Major deviations were only observed with respect to the intensity and the line width of spectra recorded in the absence of an external magnetic field. The deviations regarding the magnetic feature will be further

discussed below. The increased noise levels in these spectra is due to the fact that in these spectra temperature-dependent but non-magnetic features are also observed (vide supra).

#### 4. Discussion

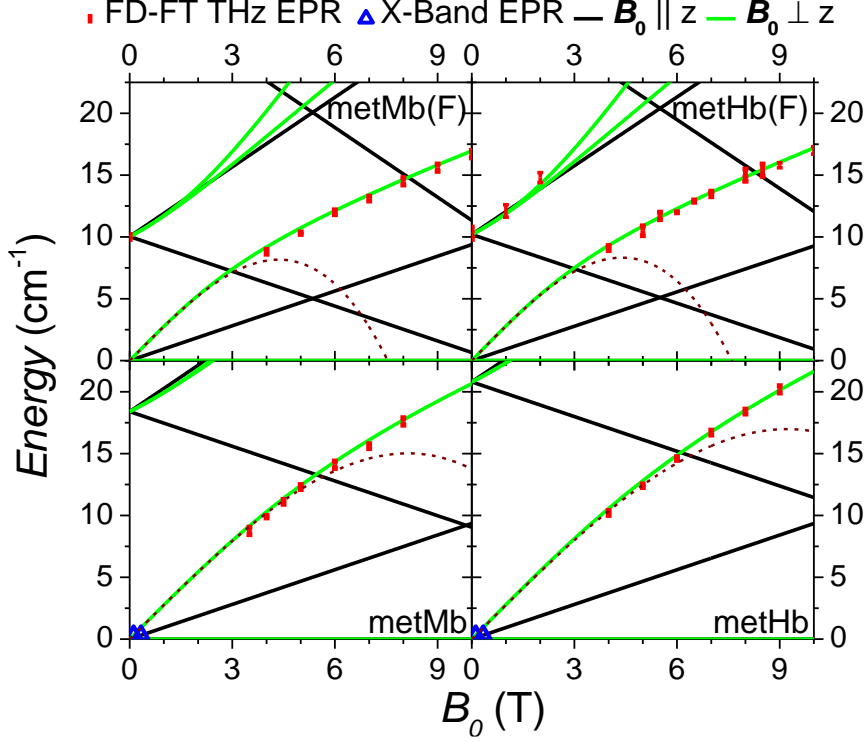


Fig. 8: Experimental EPR (red circles: FD-FT THz-EPR, blue triangles: X-band EPR) for metMb (left) and metHb (right), both with fluoro (top) and aquo (bottom) ligands. In addition, calculated  $S = 5/2$  spin energy levels are shown for parallel (black lines) and perpendicular (green lines) alignment of  $\mathbf{B}_0$  with respect to the magnetic  $z$ -axis (hard axis). Calculations were performed with SH parameters given in Tab. 1. For comparison, calculations of the ground state levels according to Eq. 5 are given (dotted lines). Energy levels are normalized to their respective ground state level.

Fig. 8 displays X-band and FD-FT THz-EPR results of metMb and metHb, with fluoro and aquo ligands, along with calculated  $S = 5/2$  levels. Spin energy levels, for parallel (black lines) and perpendicular (green lines) field alignment, were calculated with SH parameters given in Tab. 1. Sound agreement between experimental and calculated data

proves that the applied  $S = 5/2$  model and the chosen  $D$  and  $g$ -values provide robust descriptions for the magnetism of all four Fe(III) complexes.

In the following discussion we will conclude on: the observed FD-FT THz-EPR line shapes, the dependence of FD-FT THz-EPR signals on sample concentration and finally the accuracy of our ZFS values in comparison with recent studies.

Experimental field division FD-FT THz-EPR spectra of all four systems mainly reflect  $\mathbf{B}_0$  orientations perpendicular to  $z$  (see Fig. 8). This results from the line shapes of the powder transmission spectra, which determine the shapes of the field division spectra. The right panel of Fig. 5 depicts simulated metMb(F) frequency domain transmission spectra for external magnetic fields of 9 T (dashed blue) and 10 T (dashed orange). Coming from the high frequency side the transmission shows an abrupt decrease, which increases after minimum transmission at  $\mathbf{B}_0 \perp z$  (see arrows in the right panel of Fig. 5). At  $\mathbf{B}_0 \parallel z$  the transmission difference even in the simulated spectrum is nearly negligible and not detectable in the experimental spectrum.

FD-FT THz-EPR resonances were found to be unexpectedly broad. The zero field transitions in metMb(F) and metHb(F) were so broad that no precise line width parameter could be obtained. For the field dependent transitions within the  $m_S = \pm 1/2$  levels an intrinsic line width of  $0.8 \text{ cm}^{-1}$  was estimated which was found to be field independent. This finding contradicts earlier cw multifrequency (MF) EPR studies on metMb, which revealed strong field dependence of the same transition [4, 30-32]. MetMb line widths observed in this work are in good agreement with those observed at 600 GHz ( $\sim 20 \text{ cm}^{-1}$ ) and 10 T by Miyajima and coworkers [31]. However, the same study reported a line width reduction by a factor of 8, when decreasing the external magnetic field to 4 T and the frequency to 300 GHz ( $\sim 10 \text{ cm}^{-1}$ ) [31]. A possible explanation for this discrepancy could be saturation induced power broadening of FD-FT THz-EPR resonances. However,



this remains speculation at this point, as the strong overall absorption of the proteins did not allow decreasing the excitation energy

FD-FT THz EPR experiments were carried out on protein samples containing heme concentrations of 21(1) mM (metHb), 11(2) mM (metHb(F)), 20(3) mM (metMb) and 22(2) (metMb(F)), respectively. This corresponds to roughly  $10^{19}$   $S = 5/2$  heme sites in the active sample volume. For the proteins studied in the present work such high concentrations were required as FD-FT THz-EPR resonances were found to be unexpectedly broad as compared to other high spin TMI complexes (see e.g. [25-28]). In order to improve this situation protein crystals or partly ordered samples can be employed to achieve narrower EPR resonances and thereby increase the S/N.

Tab. 1: metMb and metHb SH parameters obtained in previous and present work.

Method	metMb(F)	metMb	metHb(F)	metHb	Ref.
Susceptibility	$D \sim 7 \text{ cm}^{-1}$	$D \sim 10 \text{ cm}^{-1}$			[33]
Mössbauer			$D \sim 7 \text{ cm}^{-1}, g = 2.0$		[34, 35]
Torque		$D \sim 12 \text{ cm}^{-1}$			[36]
Torque	$D = 6.5(24) \text{ cm}^{-1}$	$D = 10.5(5) \text{ cm}^{-1}$			[37]
MF EPR (10, 35 and 70 GHz)	$D = 7.0(5) \text{ cm}^{-1}, E = 0.021(7) \text{ cm}^{-1}, g_{\perp} = 1.99, g_{\parallel} = 2.00$	$D = 4.5(5) \text{ cm}^{-1}, E = 0.013(4) \text{ cm}^{-1}, g_{\perp} = 1.98, g_{\parallel} = 2.00$			[4]
MF EPR (13 and 35 GHz)		$D = 4.4(6) \text{ cm}^{-1}, g_{\perp} = 1.985(2), g_{\parallel} = 2.002(1)$			[8]

MF EPR (30-610 GHz)		$D = 9.47(5) \text{ cm}^{-1}$ , $g_{\perp} = 1.98, g_{\parallel} = 2.00$			[31]
MF EPR (70 – 400 GHz)				$D = 10.7(2) \text{ cm}^{-1}$ , $g_{\perp} = 1.95(1)$	[20]
$^{19}\text{F}$ ENDOR	$D = 5.2(1) \text{ cm}^{-1}$ (pH = 8.5), $D = 6.1(1) \text{ cm}^{-1}$ (pH=6)				[38]
X-Band EPR ( $T_i$ )	$D = 6.08(8) \text{ cm}^{-1}$	$D = 9.14(18) \text{ cm}^{-1}$			[39]
FD-FT THz EPR	$D = 5.94(8) \text{ cm}^{-1}$ , $g = 2.0$	$D = 9.5(1.5) \text{ cm}^{-1}$ , $g = 2.0$	$D = 6.30(12) \text{ cm}^{-1}$ , $g = 2.0$	$D \sim 10.5 \text{ cm}^{-1}$ estimated	[12]
FD-FT THz EPR			$D = 5.1 \text{ cm}^{-1}$ [40]		[10]
FD-FT THz EPR	$D = 5.0(1) \text{ cm}^{-1}$ , $g_{\perp} = 2.025$	$D = 9.2(4) \text{ cm}^{-1}$ , $g_{\perp} = 1.995, g_{\parallel} = 2.019$	$D = 5.1(1) \text{ cm}^{-1}$ , $g_{\perp} = 2.05(1)$	$D = 10.4(2) \text{ cm}^{-1}$ , $g_{\perp} = 1.989, g_{\parallel} = 2.018$	This work

First studies in the ZFS of metMb and metHb with fluoro and aquo ligands were based on torque [36], Mössbauer [34, 35] and susceptibility [33] measurements. These pioneering studies provided important estimates of  $D$ . Subsequent torque measurement on metMb and metMb(F) addressed the temperature dependence of  $D$  [37]. However, it was found that  $D$ -values spread out over several wavenumbers for different temperatures and crystal orientations. However, the dependence of  $D$  on the crystal orientation was not confirmed in later EPR studies [31]. In addition, extensive MF EPR work has been carried out for the determination of  $D$ . In two previous MF EPR studies, performed at two [8] respectively three [4] relatively low mw frequencies,  $D$ -values were determined on the basis of Eq. 5 for metMb [4, 8] and metMb(F) [4]. The low number of data points may

be the reason for the mismatch between  $D$ -values obtained in Refs. [4, 8] from other studies including present work (see Tab. 1). Later on, metHb was studied in one of the first high field/high frequency MF EPR studies on proteins, at several frequencies between 70 and 400 GHz.  $D = 10.7(2) \text{ cm}^{-1}$  was extracted by spectral simulations based on Eq. 5 [20], which matches our value of  $10.4(2) \text{ cm}^{-1}$ .

However, the chosen high resonance fields up to 5 T in ref. [20] may violate the low field approximation, which is a necessary condition for the validity of Eq. 5. Transition energies calculated with Eq. 5 (dotted lines in Fig. 8) clearly show the limits of this expression. For metMb(F) and metHb(F) the deviation between energy levels calculated with Eq. 5 and Eq. 1 is already more than  $1 \text{ cm}^{-1}$  at  $B_0 = 4 \text{ T}$ . For  $B_0 > 4.35 \text{ T}$  ground state splittings calculated with Eq. 5 decrease with increasing field. Such behaviour can be discarded as unphysical, hence this field can be considered as the ultimate limit for the low-field limit. Very good agreement between both models can be achieved for  $B_0 < 2 \text{ T}$ , which corresponds to  $g\mu_B B_0/D < 0.38$ . For metMb and metHb larger  $D$  values were obtained and consequently the low-field assumption is valid up to higher fields, but again the impact of higher fields is not described correctly. This restriction may be lifted by SH (Eq. 1) diagonalization for the full Hilbert space to model EPR transitions, spanning the low, intermediate and high field range. The benefits of this approach were exploited in an elaborate study by Miyajima *et al.* [31], who studied metMb single crystals by MF EPR between 37 and 608 GHz. Due to the high data quality achievable with single crystals and the density of data points measured, the obtained  $D = 9.47(5) \text{ cm}^{-1}$  constitutes the most accurate value achieved for metMb so far [31]. We determined a slightly lower  $D = 9.2(4) \text{ cm}^{-1}$ , which might be due to the slightly higher pH of the metMb solution studied by us (7.0 compared to 6.5). Nevertheless, both  $D$ -values match within experimental errors. A pH dependence of  $D$  in metMb(F) was reported by Fann *et al.*, who obtained  $D = 5.2(1)$

$\text{cm}^{-1}$  (pH = 8.5) and  $D = 6.1(1) \text{ cm}^{-1}$  (pH = 6) via pulsed  $^{19}\text{F}$  ENDOR spectroscopy [38]. Alternatively, ZFS in metMb and metMb(F) was determined by studies in the temperature dependence of the longitudinal spin relaxation time  $T_1$  [39]. Despite the fact that the determined D-values are close to the values of the present study, the applied model requires several strong assumptions, which makes an evaluation of possible errors difficult.

A study that strongly influenced the debate about ZFS in high spin heme iron proteins was the FD-FT THz-EPR study of Brackett et al. [12], which reported D-values for metMb(F), metMb and metHb(F) and estimates for metHb. The FD-FT EPR approach applied in ref. [12] is very similar to our detection technique.

The main difference of our approach consists in the application of broad band high THz CSR and significantly higher magnetic fields up to 10 T. Nevertheless, it is surprising that the D-values reported for metMb and metHb agree very well with the more accurate ones determined by us.

In both studies D-values of fluoro complexes could be determined with higher accuracy as compared to their aquo analogues. This is due to the fact that only for the fluoro states zero field transitions between  $m_S = \pm 1/2$  and  $m_S = \pm 3/2$  sublevels, which in zero field directly provide  $D$ , could be observed. For metHb and metMb similar transitions were missing. To the best of our knowledge, all previous attempts to record this transition failed (see e.g. Ref. [12]). However, based on  $D$  values determined from FD-FT THz-EPR measurements with applied magnetic field, zero field energy splittings can be calculated to  $18.4 \text{ cm}^{-1}$  (metMb) and  $20.8 \text{ cm}^{-1}$  (metHb). Due to strong broad band absorption in the protein samples this was unfortunately close to or even slightly above, the edge of the accessible energy range. Given that also for metMb(F) and metHb(F) zero field resonances were found to be very broad and weaker than expected from spectral

simulations (see lower solid blue and black dotted lines in Fig. 6a) and 6b), respectively), such transitions can be easily missed out. This is not a peculiarity of FT detected EPR. Even in Ref. [31], where metMb ( $2D = 18.4 \text{ cm}^{-1}$ ) was studied by field domain cw EPR up to 608 GHz ( $20 \text{ cm}^{-1}$ ), no signature of the  $m_S = \pm 1/2$  and  $m_S = \pm 3/2$  transition could be observed. Given the high precision of FD-FT THz-EPR to determine  $D$  in systems where zero field transitions can be directly observed, different  $D$  values reported for metMb(F) metMb(F) in [12] and in our study are surprising. The reason for this discrepancy remains unclear as both studies have been carried out at a pH of 7.0. However, in a later high quality FD-FT THz-EPR study on metHb(F)  $D = 5.1 \text{ cm}^{-1}$  [10] was found. Hence, we concluded that at least for metHb(F) the  $D$ -value determined by us is more accurate.

## 5. Conclusion

Based on a novel combined X-band and FD-FT THz-EPR approach together with diagonalization-based field/frequency domain EPR simulations, we were able to determine axial ZFS in heme  $S=5/2$  states of metMb(F), metMb, metHb(F) and metHb. Benefiting from the accuracy of our approach we were able to confirm recent ZFS values in metMb(F) and metMb. For metHb and metHb(F) ZFS values with improved accuracy could be provided. Our results summarized in Tab. 1. set important bench marks for future quantum chemical calculations (e.g. density functional theory calculations [15, 16]) for an improved understanding of magnetic and electronic structures of the investigated Fe(III) states and other heme proteins. The present study shows the potential of FD-FT THz-EPR for the investigation of HS TMI in frozen protein solutions. It sets the basis for future FD-FT THz-EPR studies on other important metalloproteins with HS TMIs as functional units (e.g. Fe(II), Mn(III), Mn(IV), Co(II), Co(III) and Ni(II)). This is of particular importance, as these systems contain many cases which have been inaccessible to EPR spectroscopy until now. However, the applicability of this approach could be

further increased by increasing its detection sensitivity. Major improvements with respect to detection sensitivity and precision of the extracted SH parameters should be achieved by improved quasi optical detection schemes and the employment of proteins crystals. Corresponding work is under way in our labs.

**Acknowledgement:** This work has been supported and funded by DFG priority program SPP 1601. BMM is supported by DFG (MA 3348/2-2). FD-FT THz-EPR has been carried out within the BESSY II user program. We thank Sun Un (CEA, Saclay) for helpful discussions and Dirk Ponwitz (HZB) for technical support.

## References

- [1] B. A. Wittenberg and J. B. Wittenberg, *Annu. Rev. Physiol.* **51**, 857 (1989).
- [2] H. Mairbäurl and R. E. Weber, in *Comprehensive Physiology* (John Wiley & Sons, Inc., 2011).
- [3] J. Yi, L. M. Thomas and G. B. Richter-Addo, *Acta Crystallogr. F* **67**, 647 (2011).
- [4] E. F. Slade and R. H. Farrow, *Biochim. Biophys. Acta* **278** (3), 450 (1972).
- [5] J. Krzystek, A. Ozarowski and J. Telser, *Coord. Chem. Rev.* **250** (17-18), 2308 (2006).
- [6] D. J. E. Ingram and J. C. Kendrew, *Nature* **178** (4539), 905 (1956).
- [7] D. J. E. Ingram, J. F. Gibson and M. F. Perutz, *Nature* **178** (4539), 906 (1956).
- [8] P. Eisenberger and P. S. Pershan, *J. Chem. Phys.* **45** (8), 2832 (1966).
- [9] C. J. Cramer and D. G. Truhlar, *Phys. Chem. Chem. Phys.* **11** (46), 10757 (2009).
- [10] P. M. Champion and A. J. Sievers, *J. Chem. Phys.* **72** (3), 1569 (1980).
- [11] J. Telser, J. van Slageren, S. Vongtragool, M. Dressel, W. M. Reiff, S. A. Zvyagin, A. Ozarowski and J. Krzystek, *Magn. Reson. Chem.* **43**, S130 (2005).
- [12] G. C. Brackett, P. L. Richards and W. S. Caughey, *J. Chem. Phys.* **54** (10), 4383 (1971).
- [13] D. Gatteschi, A. L. Barra, A. Caneschi, A. Cornia, R. Sessoli and L. Sorace, *Coord. Chem. Rev.* **250** (11-12), 1514 (2006).
- [14] A. Bencini and D. Gatteschi, *EPR of exchange coupled systems*. (Springer Verlag, Berlin, 1990).
- [15] F. Neese, in *Calculation of NMR and EPR Parameters. Theory and Applications*, edited by M. Kaupp, M. Bühl and V. G. Malkin (Wiley-VCH, Weinheim, 2004), pp. 541.
- [16] R. Boca, *Coord. Chem. Rev.* **248** (9-10), 757 (2003).
- [17] J. R. Pilbrow, *Transition Ion Electron Paramagnetic Resonance*. (Clarendon Press, Oxford, 1990).
- [18] N. M. Atherton, *Principles of Electron Spin Resonance*. (Ellis Horwood, New York, 1993).
- [19] S. Stoll and A. Schweiger, *J. Magn. Reson.* **178** (1), 42 (2006).

- [20] Y. Alpert, Y. Couder, Tuchendl.J and H. Thome, *Biochim Biophys Acta* **322** (1), 34 (1973).
- [21] A. Schnegg, J. Behrends, K. Lips, R. Bittl and K. Holldack, *Phys. Chem. Chem. Phys.* **11** (31), 6820 (2009).
- [22] B. Seamonds, R. E. Forster and P. George, *J. Biol. Chem.* **246** (17), 5391 (1971).
- [23] M. Abo-Bakr, J. Feikes, K. Holldack, P. Kuske, W. B. Peatman, U. Schade, G. Wüstefeld and H. W. Hübers, *Phys. Rev. Lett.* **90** (9), 094801 (2003).
- [24] M. Bolognesi, S. Onesti, G. Gatti, A. Coda, P. Ascenzi and M. Brunori, *J. Mol. Biol.* **205** (3), 529 (1989).
- [25] K. S. Pedersen, J. Dreiser, J. Nehrkorn, M. Gysler, M. Schau-Magnussen, A. Schnegg, K. Holldack, R. Bittl, S. Piligkos, H. Weihe, P. Tregenna-Piggott, O. Waldmann and J. Bendix, *Chem. Commun.* **47** (24), 6918 (2011).
- [26] J. Dreiser, A. Schnegg, K. Holldack, K. S. Pedersen, M. Schau-Magnussen, J. Nehrkorn, P. Tregenna-Piggott, H. Mutka, H. Weihe, J. Bendix and O. Waldmann, *Chem. Eur. J.* **17** (27), 7492 (2011).
- [27] J. Dreiser, K. S. Pedersen, A. Schnegg, K. Holldack, J. Nehrkorn, M. Sigrist, P. Tregenna-Piggott, H. Mutka, H. Weihe, V. S. Mironov, J. Bendix and O. Waldmann, *Chemistry – A European Journal* **19** (11), 3693 (2013).
- [28] A. P. Forshaw, J. M. Smith, A. Ozarowski, J. Krzystek, D. Smirnov, S. A. Zvyagin, T. D. Harris, H. I. Karunadasa, J. M. Zadrozny, A. Schnegg, K. Holldack, T. A. Jackson, A. Alamiri, D. M. Barnes and J. Telser, *Inorg Chem* **52** (1), 144 (2012).
- [29] A. M. F. Benial, M. K. Dhas and A. Jawahar, *Appl. Magn. Reson.* **40** (3), 311 (2011).
- [30] P. J. M. van Kan, E. van der Horst, E. J. Reijerse, P. J. M. van Bentum and W. R. Hagen, *Journal of the Chemical Society, Faraday Transactions* **94** (19), 2975 (1998).
- [31] Y. Miyajima, H. Yashiro, T. Kashiwagi, M. Hagiwara and H. Hori, *J. Phys. Soc. Jpn.* **73** (1), 280 (2004).
- [32] E. F. Slade and D. J. E. Ingram, *Nature* **220** (5169), 785 (1968).
- [33] A. Tasaki, J. Otsuka and M. Kotani, *Biochim. Biophys. Acta* **140** (2), 284 (1967).
- [34] G. Lang and W. Marshall, *J. Mol. Biol.* **18** (3), 385 (1966).
- [35] G. Lang and W. Marshall, *Proc. Phys. Soc. London* **87** (555P), 3 (1966).
- [36] H. Morimoto, T. Iizuka, J. Otsuka and M. Kotani, *Biochim Biophys Acta* **102** (2), 624 (1965).
- [37] H. Uenoyama, T. Iizuka, H. Morimoto and M. Kotani, *Biochim. Biophys. Acta* **160** (2), 159 (1968).
- [38] Y. C. Fann, J. L. Ong, J. M. Nocek and B. M. Hoffman, *J. Am. Chem. Soc.* **117** (22), 6109 (1995).
- [39] C. P. Scholes, R. A. Isaacson and G. Feher, *Biochim. Biophys. Acta* **244** (1), 206 (1971).
- [40] zero-field transition at 10.2 cm<sup>-1</sup> (correspond to : D = 5.1 cm<sup>-1</sup>)